AGU100 ADVANCING EARTH AND SPACE SCIENCE

Geophysical Research Letters

RESEARCH LETTER
10.1029/2019GL084241

Infragravity Wave Generation by Wind Gusts

T. Vrećica[1], R. Soffer[1], and Y. Toledo[1]

[1]School of Mechanical Engineering, Tel-Aviv University, Tel Aviv, Israel

Key Points:
- We discovered evidence of significant deep water infragravity wave generation by analyzing ADCP and pressure cell measurements
- We found new nonlinear mechanisms to generate IG waves in the deep ocean connecting wind waves with winds, gusts, or deep bathymetry features
- We show how the new findings explain dual peaked IG spectrum measurements and compensate for large underestimations observed in the Pacific

Supporting Information:
- Supporting Information S1

Correspondence to:
Y. Toledo,
toledo@tau.ac.il

Citation:
Vrećica, T., Soffer, R., & Toledo, Y. (2019). Infragravity wave generation by wind gusts. *Geophysical Research Letters*, *46*, 9728–9738. https://doi.org/10.1029/2019GL084241

Received 4 JUL 2019
Accepted 30 JUL 2019
Accepted article online 5 AUG 2019
Published online 16 AUG 2019

Abstract Through the analysis of propagation times of infragravity wave packets along ray paths, reanalysis data, and our field measurements in the East Mediterranean, we find evidence of deep water infragravity wave generation by offshore storms. We confirmed the results also using deep water pressure cell measurements in the Pacific. The known nearshore generation mechanism showed large discrepancies with the observed infragravity energy near Aogashima, Japan, during winter. A new model of deep water infragravity wave generation is developed, based on nonlinear interactions of wind wave triads with submesoscale wind oscillations. The observed underprediction of infragravity waves is resolved using this new gustiness-based model. The new source term is found to be of importance during strong storms in the open ocean and underlines the importance of accounting for submesoscale wind oscillations in wind wave models.

Plain Language Summary Ocean infragravity waves are surface waves with periods, lengths, and speeds much greater than the ones of wind waves and lower than those of tides. The primary generation mechanisms are related to shoaling and breaking of nearshore wind waves. A common assumption is that the origin of deep water infragravity waves is the reflection from near or far coastlines. By analyzing pressure cell measurements and wind and wave model data, we found evidence that deep water generation mechanisms also play a significant role. We present a new process connecting seemingly unrelated phenomena of the comparably slow wind gusts and very fast infragravity waves through nonlinear resonances. Its implementation compensated for underestimations of modeled infragravity waves in deep waters of the Pacific. Besides additional energy, the newly found mechanisms introduce also new frequencies and directional properties which may play a significant role in numerous situations. Infragravity waves are the main cause of harbor resonances. They are also related to various other fields such as sediment transport, altimetry measurements, wave-ice sheet interactions, and Earth's hum.

1. Introduction

Infragravity (IG) waves are an interesting physical phenomenon remarkably similar to tsunamis in deep waters, while their amplitudes are much smaller. They are thought to affect altimetry measurements (Ardhuin et al., 2014) and are coupled to various physical processes such as sediment transport (Aagaard & Greenwood, 1994), breaking of ice sheets in the Pacific (Bromirski et al., 2010), and the Earth's hum (Rhie & Romanowicz, 2006). They are also detrimental for harbor design as they can resonate within its bounds (Zhang et al., 2016). While the study of IG waves has been ongoing for a long time (Tucker, 1950), only recently was it extended to deep waters (Aucan & Ardhuin, 2013; Godin et al., 2013) due to technical difficulties of measuring these waves at large depths. There are various known nearshore IG waves generation mechanisms, as discussed in Herbers et al. (1994, 1995); Schäffer (1993); Symonds et al. (1982); Longuet-Higgins and Stewart (1962). Some deep water mechanisms are known and explored in Sugioka et al. (2010), Uchiyama and McWilliams (2008), and de Jong and Battjes (2004). A common assumption is that the source of deep water IG waves is the reflection of the nearshore generated IG waves from far coastlines. The operational reflection model (Ardhuin et al., 2014) treats all coastlines as sources of IG waves, which generate uniformly distributed IG waves spectra. This approach was shown to be able to account for the observed IG waves in most cases. Nevertheless, it does not account for the observed IG wave properties in certain events which are discussed here.

We show that storm conditions induce nonlinear deep water IG wave generation through interaction of three waves and oscillations of wind speed. This is somewhat of a paradigm shift, as wave triads are assumed not

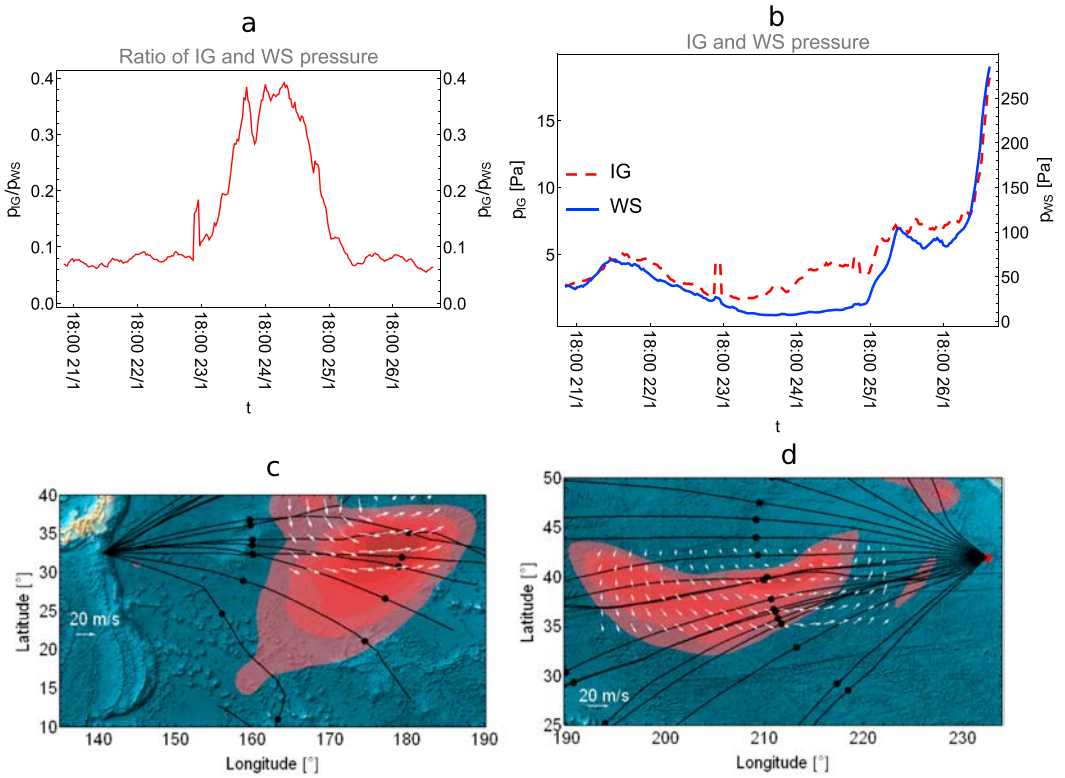

Figure 1. (a) Ratio and (b) absolute values of the IG wave pressure response and wind sea pressure response, obtained using a pressure cell deployed at 24-m depth near Haifa, Israel. (c) Ray paths of a 100-s wave originating from the Aogashima array. (d) Ray paths of a 150-s wave originating from the midpoint of the Cascadia array. The semitransparent red color map serves as an indicator of relative distribution of wave energy in the heart of the storm (10% per color level), and the maximal values were 40 and 10 m^2, respectively. Black dots indicate 6-hr propagation time, and white arrows indicate mean wind speeds. IG = infragravity; WS = wind sea.

to provide a mean energy transfer between waves in deep water (Hasselmann, 1962) without the presence of a current. Unlike other deep water mechanisms, our model also predicts IG wave generation in both directions with respect to the wind and mostly at different frequencies than known generation mechanisms. This new mechanism provides a plausible explanation for the IG waves arriving from far sources, with no apparent storms at far coastlines. An observed underprediction of IG wave heights in the Pacific (Tonegawa et al., 2018) was accounted for using the new model.

2. Observations of IG Waves Arriving From Far Sources

We first analyzed Acoustic Doppler Current Profiler measurements in the East Mediterranean basin. The processing of the time series recorded by the pressure cell shows that the ratio of the observed IG waves and wind sea (0.05 to 0.2 Hz in this case) pressure density ($p_{IG} = \int_{0.004}^{0.05} P_f \mathrm{d}f, p_{WS} = \int_{0.05}^{0.2} P_f \mathrm{d}f$) remained mostly constant during the measurement campaign. This indicates that the generation of IG waves during shoaling is linearly proportional to the wind sea (about 7% in our case) and is inline with many previous observations (Herbers et al., 1994, 1995).

However, a peak of 40% was observed on 24 January 2017 (Figure 1a). As it is impossible to generate IG waves of such ratio during shoaling, the observed IG waves must have arrived from a far source. The values of pressure response of wind sea are shown together with the IG wave pressure response (Figure 1b). This shows that there is some IG energy present that cannot be explained by local conditions.

The East Mediterranean basin is relatively small with a structure which permits more complex shore reflection patterns and trapped mode effects specifically in nearshore measurements (see Smit et al., 2018with respect to significant trapped IG energy content). Therefore, we examine the data from deep ocean measurement campaigns to further investigate this theory without these possible factors. Several events where

IG waves arrived from far sources have been observed in the eastern Pacific by deep water differential pressure gauges of the Cascadia measurement array (Figure S1a in the supporting information). Directional properties of the IG wave field were recovered, using an array of differential pressure cells (Neale et al., 2015).

We also investigate a more recent analysis of IG waves which was done using a measurement obtained by an array of absolute pressure gauges about 70 km off the coast of Aogashima (Figure S1b), Japan (Tonegawa et al., 2018). The modeled and measured significant IG wave heights during the summer months were mostly in agreement. However, during the winter months (most notably during January and February), a major increase of IG wave energy was observed, which is not accounted for by reflection from coasts by the hindcast model of Ardhuin et al. (2014). Here we also use hindcast data, and we perform our own processing of the raw Aogashima data to further investigate the IG wave properties. This data set is the focus of this work as it provides the most comprehensive information.

3. Theory and Methods

3.1. Instrumentation and Processing Methodology

We deployed an Acoustic Doppler Current Profiler equipped with an acoustic surface tracking beam and a pressure cell 2.7 km offshore Haifa, at a depth of 24 m. Measurements were continuously collected during at a sampling frequency of 4 Hz. The midpoint of the Aogashima array (station A05) is used as a reference point in the Pacific measurements. It was deployed at 1,762-m depth and also has sampling frequency of 4 Hz. As we seek to obtain only high accuracy measurements, a cutoff frequency of 0.02 Hz was deemed appropriate, based on the linear theory and signal-to-noise ratio as shown in Tonegawa et al. (2018). Linear transfer functions were applied on both pressure measurements.

For all pressure cells under consideration we first filter out the effects of tides. A Fourier transform is then applied to each pressure record yielding pressure density spectra (P_p). The amplitude energy spectra (E_p) is obtained by taking the absolute value of the pressure density spectrum, multiplying it by the ratio of pressure decay divided by water density multiplied by gravity, squaring this quantity, and normalizing output

$$E_p = \frac{1}{N}\left(|P_p|\frac{\cosh kh}{\rho g}\right)^2, \tag{1}$$

where N is the normalizing factor. The significant wave height of IG waves is defined as 4 times the square root of the variance in the sought frequency range

$$H_{\mathrm{IG}} = 4\sqrt{\int_{0.005}^{0.02} E_{f'}\mathrm{d}f'}. \tag{2}$$

3.2. Basic Properties of Nonlinear Interactions

Ocean surface waves propagate according to the dispersion relation: $(2\pi f)^2 = gk\tanh(kh)$, where ω is the angular frequency, k is the wavenumber, g is the gravitational acceleration, and h is the local water depth. Due to the nature of the dispersion relation in deep water conditions, it is impossible for three wave interactions to resonate, both in spatial ($k_1 = k_2 \pm k_3$) and temporal ($f_1 = f_2 \pm f_3$) domains. However, various inhomogeneities of the wave field in space and time are able to act as an additional component (k_b) to close a Bragg resonance condition ($k_1 = k_2 \pm k_3 + k_b$). This is one of the reasons IG waves are generated in a shoaling process; the sea bottom changes can act as an additional component. To account for such inhomogeneities, some of the most common assumptions such as averaging the wind speeds over long distances are reevaluated.

We note that there are other mechanisms of nonlinear IG waves generation in deep water (de Jong & Battjes, 2004; Sugioka et al., 2010; Uchiyama & McWilliams, 2008). While these mechanisms play a role in overall IG wave generation, they usually create waves at different scales than those considered here (submesoscale). Unlike other models, our model also predicts IG wave generation in both directions with respect to the wind.

The wind wave field evolution is commonly modeled using wind speeds averaged over the temporal and spatial scales of the model (Janssen, 2004). The mean wave growth due to subgrid wind speed changes is parametrized. Typical gusts during storms can be well described by a white noise spectrum (see Abdalla & Cavaleri, 2002). In this paper, we consider gusts in frequencies ranging from 0.004 to 0.1 Hz. LIght Detection And Ranging measurements show that the wind speeds are highly correlated between two points lying in

the mean wind direction. This correlation quickly decays as the angle between the mean direction and the two points increases (Simley et al., 2012).

The wavelength of wind gust oscillations capable of closing Bragg resonance is in the order of 1 km. Assuming the gusts propagate at the mean wind speed, the periods capable of closing resonance are 1–3 min. Such periods can correspond to general gust frequencies. Accounting for gust effects results in uneven growth of the wave field, essentially a modulation of the free surface, which can close the Bragg resonance. This is similar in nature to the free surface modulations in coastal waters due to bottom ripples.

3.3. Reconstruction of the Atmospheric and Ocean Conditions Along Ray Paths

To determine the direction of IG waves propagation, we have coded a dedicated ray tracing method. In operational models, the method of propagation around great circles is usually used to trace the path of a wave in a longitude-latitude coordinate system. For IG waves, it is also necessary to take into account the refraction of the wave rays due to bathymetry changes. We define the water depth as a function of longitude and latitude using the ETOPO1 data (Amante & Eakins, 2009). Latitude, longitude, and direction of propagation are a system of ordinary differential equations (see The Wamdi Group, 1988) and are solved using Mathematica[ĭ] NDSolve function with a 1-s time step. Usually, the bathymetry is smoothed, or a very large spatial step is taken to avoid inherent problems of ray tracing (the solution is only valid for mild changes; see Thomson et al., 2007). Here, we use a more detailed bathymetry for the numerical simulations, with 5' resolution and 1' smoothing. This only accounts for bathymetry elements which are on the scale of typical IG wavelenghts.

The archived European Centre for Medium-range Weather Forecasts ERA-interim, and ERA5 reanalysis data have been used to define sea state conditions (significant wave height, mean wave direction, mean wave period, horizontal components of wind speed at 10 m, peak gustiness at 10 m, convection velocity, and Charnock coefficient) as functions of space and time (Dee et al., 2011). The reanalysis data have a (1/4)° spatial resolution in a longitude-latitude coordinate system and temporal resolution of 6 hr. Linear interpolation has been employed to extrapolate values between grid points in both space and time.

The energy density spectra are defined as a function of frequency (f) and direction (θ) as $S(f,\theta) = F(f)P(f,\theta)$, in such a way that the total energy density corresponds to the modeled significant wave height, peak direction, and peak frequency. $F(f)$ represents the total energy density distribution, $P(f,\theta)$ is the directional spread function, and $S(f,\theta)$ is the wave spectrum. Since this work aims at investigating basic properties of IG waves generation, a rather simple definition of the spectrum is used. We assume that $S(f,\theta)$ has the shape of a JONSWAP spectrum (Hasselmann et al., 1973) and cosine-square directional spreading, $P(f,\theta) = \cos^2(\theta_m - \theta)$, where θ_m is the mean wave direction.

3.4. The Nonlinear Gustiness Wave Model

As the exact phasings of the wave field are unknown, its evolution is simulated using the wave action equation (WAE). It describes propagation and evolution of the wave action in time and space, while discarding the information on the phasings. We assume that the wind sea is not affected by IG waves, due to their small amplitudes. Following the previous work of the authors (Vrecica & Toledo, 2016), the WAE for IG wave components can be defined as

$$\frac{\partial E_p}{\partial t} + \nabla \cdot (C_{g,p} E_p) = D_p E_p C_{g,p} + S_{p,nl,3}, \tag{3}$$

where the subscript p indicates frequency for all variables, a_p is the wave amplitude, $E_p = a_p a_{-p}$ is the spectral component at frequency $f_p = p f_{\min}$ ($f_{\min} = f_1$ is the lowest frequency under consideration), $C_{g,p}$ is the group velocity, and $S_{p,nl,3}$ is the nonlinear triad source term for IG wave components due to gustiness. Originally, the D_p term represented a dissipation of wave energy; however, it can also describe the energy input. In this paper it accounts for wave growth due to wind forcing.

The formulation for generation of IG waves by gustiness assumes that waves are able to close resonance with wind gusts, similarly to how waves interact with bottom ripples in coastal areas. As the wind speed oscillates in time and space, so does the growth rate incorporated inside the D_p term. In order to account for this behavior, the model of Vrecica and Toledo (2016) is adapted to evaluate the evolution of the wave field along characteristic lines ($s = t + C_{g,p}x$), which follow the wave propagation in time and space. This results

in a formulation of the WAE nonlinear triad source term fitting for the estimation of IG wave generation by resonant gust-triad interactions

$$S_{p,nl,3} = 2\sum_{r=-\infty}^{\infty} W_{r,r-p} e^{i\int_0^s D_r + D_p + D_{r-p}\mathrm{d}s'} \times \times \int_0^s W_{-r,-r+p} E_r E_{r-p} e^{-i\int_0^{s'} D_r + D_p + D_{r-p}\mathrm{d}s''}\mathrm{d}s' = 2\sum_{r=-\infty}^{\infty} R(\theta_{\mathrm{IG}} - \theta_w)(V_r E_{r,\mathrm{res}} E_{r-p} + V_{r-p} E_r E_{r-p,\mathrm{res}}) + \mathrm{Oscill.Term.} \quad (4)$$

Here, $E_{r,\mathrm{res}}$ and $E_{p-r,\mathrm{res}}$ are the spectral components which close resonance, W term is the nonlinear interaction coefficient in operator form, and the V term is the nonlinear interaction coefficient evaluated for resonant components. The oscillatory term represents bound waves and is discarded. The R term indicates the directional spreading of generated IG wave energy. In this paper it is assumed that it is evenly distributed, as was also done in Ardhuin et al. (2014). The definition of the R and V terms can be found in the supporting information.

Let us inspect equation (4). To illustrate how, in the presence of wind gusts, a wave triad resonance can be closed, consider a solution of the linear WAE for a wind wave harmonic

$$E_p(s) = E_p(0) e^{\int_0^s C_{g,p} D_p \mathrm{d}s'}. \quad (5)$$

If the growth rate (D_p) oscillates at a certain frequency, so too will a part of the wind wave component. This oscillation in wave energy can provide the necessary component required for closing the resonance condition.

The oscillations of wind speed are modeled according to the white noise spectral shape (Abdalla & Cavaleri, 2002). This spectra represents expected gust properties averaged over a long time. While there may be deviations from it, these will average out over a large number of ray paths and travel times. As these gusts are mostly measured in one location, it is assumed that for a short distance they propagate as waves which travel at mean wind speed (U). This allows to define their spatial wavenumber.

To estimate the resonant component of wave spectra (for example $E_{r,\mathrm{res}}$) for every triad wave interaction, we consider only gust components (k_G) which modulate E_r in such a way that they close the near resonance ($\boldsymbol{\alpha} + \mathbf{k}_\mathbf{p}^{\mathbf{IG}} = \mathbf{k_r} - \mathbf{k_{r-p}} \pm \mathbf{k_G}$) with $-0.1k_{67} \le |\alpha| \le 0.1k_{67}$, where k_{67} corresponds to wavenumber of 67-s wave, which lies in the center of frequency range of interest. The spectra of wind oscillations, $S_G(f)$, are integrated between these near-resonant frequencies to yield

$$G = \sqrt{\int_{f_a}^{f_b} S_G(f)\mathrm{d}f / W}. \quad (6)$$

f_a and f_b are the frequencies of gusts which are taken into account (corresponding to the wavenumber mismatch of α outlined in previous paragraph), and W is the total gust variance. The G term represents the resonant gust component and $S_G(f)$ represents the gustiness spectrum, which is taken as a constant white noise within 0.004–0.1 Hz).

Consider the spectral terms inside the integral of equation (4). They will oscillate proportionally to the G term. The phasings of the gust components will quickly evolve, so the correlation between gusts and wind waves depends on relatively short time scales (which is why E_r can be assumed as constant). Based on the data considered in this paper, here we assume that correlation builds over distances which a $T_1 = 67$-wave crosses in 250 s. The correlation time with respect to IG wave frequency will be $t_{\mathrm{cor}} = 250\, C_{g,p}/C_g(T_1)$.

The part of the wind wave component E_r which oscillates at the frequency that closes resonance corresponds to a difference of growth rates over time t_G. During this time the wave propagates the distance ($L_G = 2\pi/k_G$) corresponding to the wavenumber mismatch $t_G = L_G/C_{g,r}/2 = \pi/k_G/C_{g,r}$. This difference rate is hence given by

$$E_{r,\mathrm{osc}} = \int_{f_{r-1/2}}^{f_{r+1/2}} \int_{\theta_a}^{\theta_b} \left(\gamma(u^* + 0.5\sigma_G) - \gamma(u^* - 0.5\sigma_G)\right) \frac{t_G}{2} S(f,\theta)\mathrm{d}f\,\mathrm{d}\theta, \quad (7)$$

where γ represents the wave growth due to wind forcing, u^* is friction velocity, and σ_G represents the standard deviation of friction velocity proportional to wind gusts, $\sigma_G = \sigma^* G$. For simplicity and without a significant loss in accuracy, the difference rate can be assumed as constant within the spectral bin and equation (7) can be written as a multiplication with a spectral component (E_r).

The above terms were defined in Janssen (2004) and are commonly used in operational models in order to account for mean wave growth due to gustiness effects; see Part VII : ECMWF Wave Model (2018). The oscillatory behavior of wind gustiness can be parametrized in various ways. Here, an oscillatory wave growth was developed using the same parametrization in order to allow for consistency in gustiness modeling which uses the available input parameters used in operational models.

Finally, the resonant component $E_{r,\mathrm{res}}$ is obtained by multiplying the interaction term, correlation time, and oscillatory component as follows:

$$E_{r,res} = t_{\mathrm{cor}} V_r E_{r,\mathrm{osc}}. \tag{8}$$

The interacting wind wave component, for example E_{r-p}, is obtained by integrating the directional wave spectra in the narrow directional band ($\pm 1°$ in this paper) around the mean wind direction (θ_m)

$$E_{r-p} = \int_{f_{r-p-1/2}}^{f_{r-p+1/2}} \int_{\theta_m - 1°}^{\theta_m + 1°} S(f, \theta) \mathrm{d}\theta \mathrm{d}f. \tag{9}$$

There are two interesting points to consider. It is possible to generate waves propagating in the opposite direction to the wind; we simply choose different wavelength of gustiness ($-k_1 = k_2 - k_3 + k_G$ instead of $k_1 = k_2 - k_3 + k_G$). This situation is expected to be the norm because these two gust wavelengths are similar due to the very IG wave component k_1. Second, the same reasoning implies that it is possible to generate IG waves by gusts in all directions not just in the mean wind direction as a small directional difference in the gust component or the wind wave components results in a significant directional change of the small IG wavenumber vector.

4. Numerical Simulations

4.1. Ray Tracing

A ray tracing approach is used to interpret measurements that may indicate offshore IG generation in the Pacific. In (Figure 1c) we show a typical event for the Aogashima array, on 19 February. In order to determine potential source locations of IG waves for the 5 May event (see Neale et al., 2015), propagation paths of 150-s IG waves in space (Figure 1d) have been determined. The wind sea conditions in the storm area (including wind speeds and relative distribution of wave variance) are also shown.

The ray paths of 200-, 100-, 67-, and 50-s waves, originating from the midpoint of the Aogashima array, are simulated (50- and 67-s rays are shown in Figures 2a and 2b). The propagation times are 25, 33.33, 41.67, and 50 hr, respectively. Only wave rays that propagate into the open ocean are considered. Their evaluation stops if the water depth in the open ocean becomes shallower than 250 m. They are calculated with a 2° step, and a total directional spread of 100° is assigned to each frequency (corresponding to spreading of waves that propagate from deep water onto the continental shelf). Simulation of IG wave generation is performed along these rays in the following subsection.

4.2. Modeling IG Wave Generation Along Ray Paths

An underestimation of significant IG wave height in the results of the nearshore generation-reflection model is observed during winter, while the model performed much better during summer. Therefore, we completed simulations for the months of January and February 2015 (periods of highest underestimation) and for June 2014 (where it performed well). The generation of IG wave components is simulated using equation (4) along ray paths of 200-, 100-, 67-, and 50-s waves. Values of the gustiness source term are shown for selected wave rays (Figures 2c and 2d) during 22 January. Wind sea conditions are shown in Figures S2a and S2b for this period. The values of significant IG wave heights obtained from the measurements, modeled by the reflection model and modeled by the combined reflection-gustiness model, are shown during the winter months (Figure 2e) and during the summer months (Figure 2f).

4.3. Comparison of Measured and Modeled IG Wave Spectra

To gain a more in-depth understanding of IG wave properties, measured and modeled spectra are presented in Figure 3. The measured IG wave spectra show rapid oscillations (observed also in Mediterranean

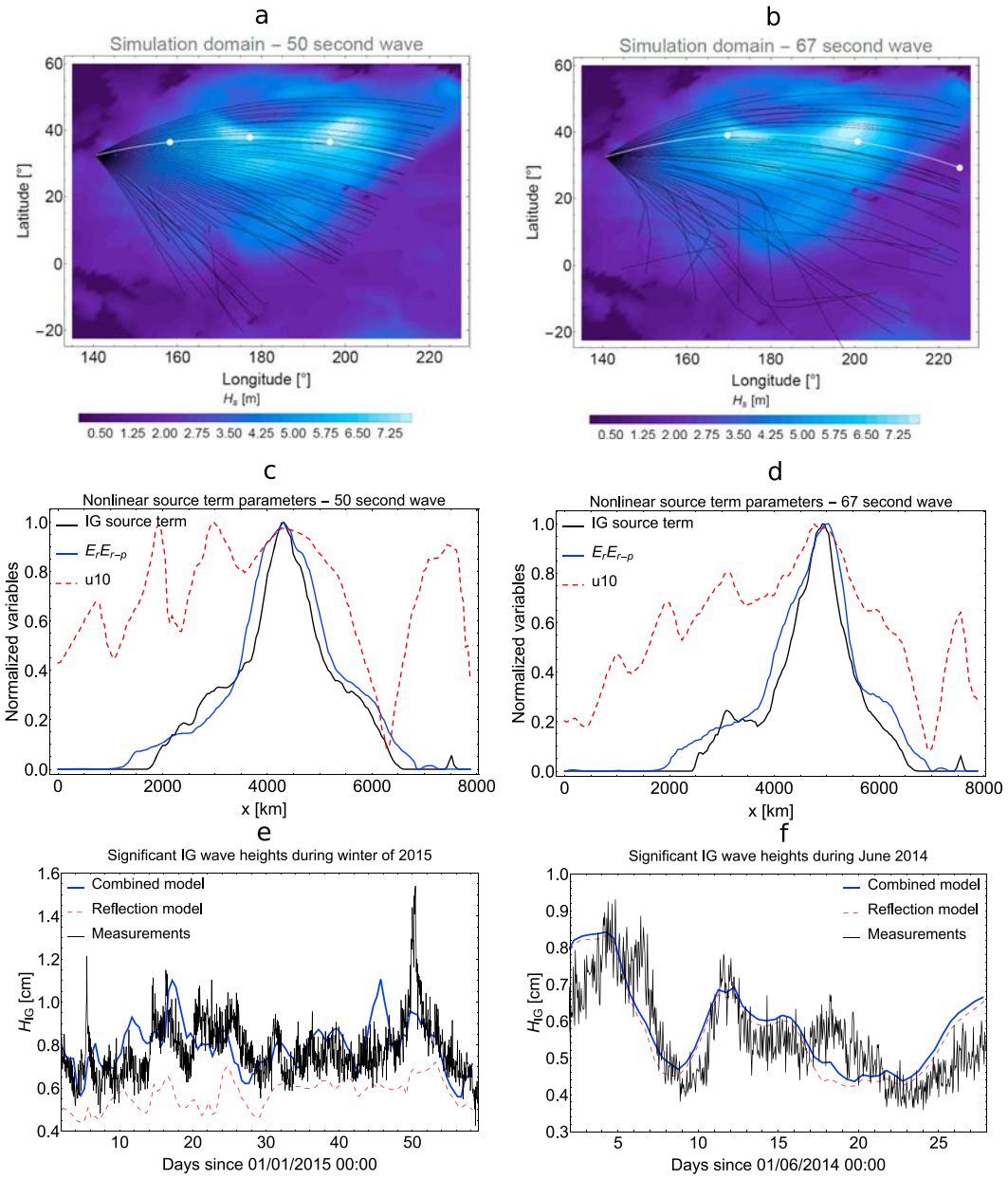

Figure 2. Ray paths of a (a) 50- and (b) 67-s wave originating from the midpoint of the Aogashima array. The wave rays are calculated with a 2° step; the white dots indicate 12-hr travel time. Values of gustiness source term, wind speed, and multiplication of spectral components contributing the most toward generation are normalized by their maximal values (2.6×10^{-11} m^2 , 18 m/s, 6.3×10^{-7} m^2 for 50-s wave and 2.4×10^{-11} m^2 , 17.5 m/s, 6.4×10^{-7} m^2 for 67-s wave) and plotted along white ray paths that are also shown for (c) 50- and (d) 67-s IG wave ray paths. Results are obtained using equation (4) for 21 January at 24:00. Measured (black line, 1-hr resolution) and modeled (dashed red line—reflection model and blue line—combined model) significant IG wave height in 50- to 200-s range at Aogashima array is shown for winter (e) and summer months (f). The simulation of IG wave generation is performed along ray paths of a 0.005-, 0.01-, 0.015-, and 0.02-Hz waves originating from the midpoint of the Aogashima array. IG = infragravity.

measurements, and in Tonegawa et al., 2018), which can be deduced from the plot of significant IG wave heights. Therefore, we show the running mean of measured IG wave spectra in Figure 3a, the one obtained by the combined reflection-gustiness model during winter months in Figure 3b, and the spectra obtained by the individual source terms are shown in Figures 3c and 3d. The averaged values of measured and modeled (all three variants) IG wave spectra are shown for winter (Figure 3e) and summer (Figure 3f).

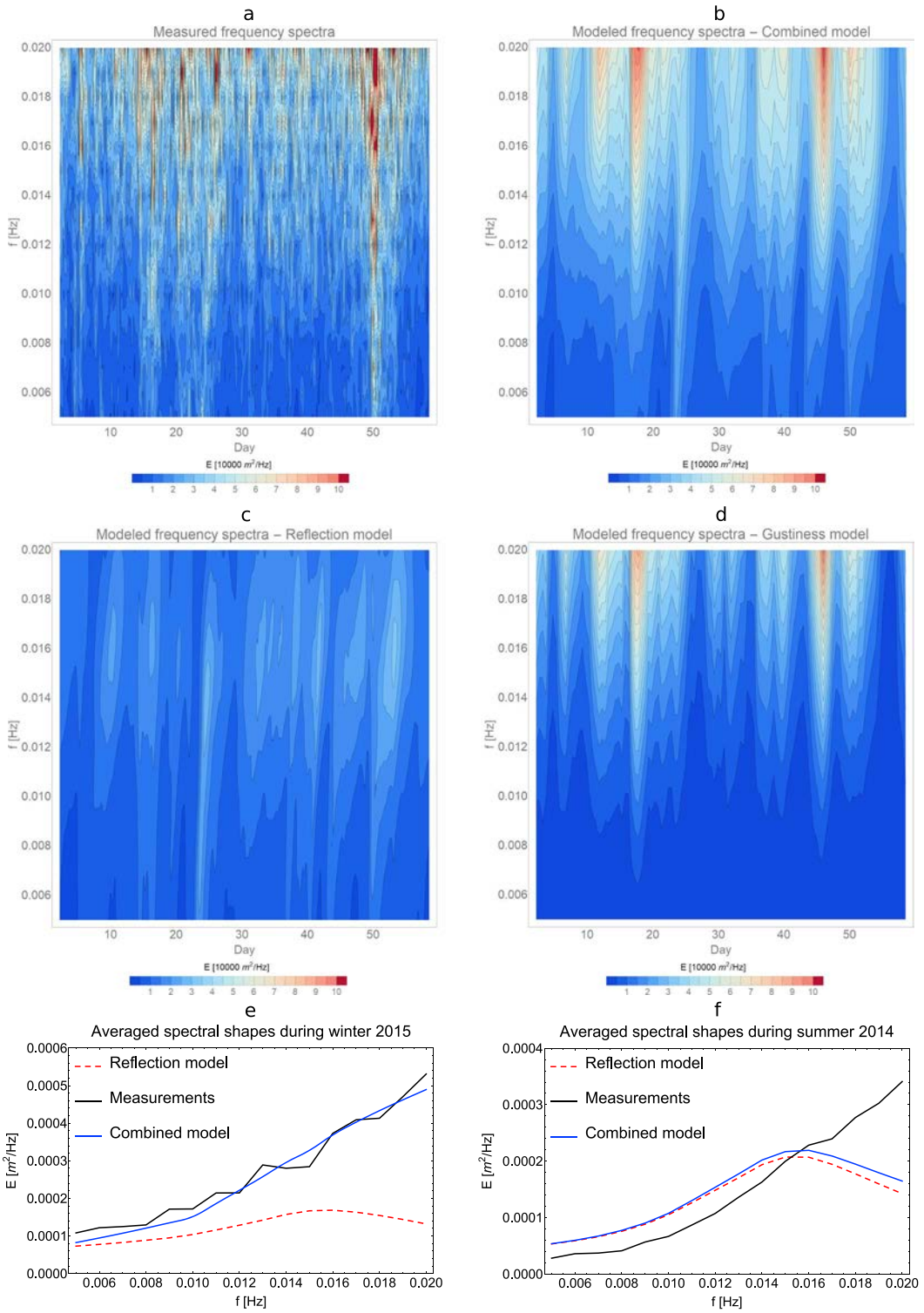

Figure 3. A comparison of measured and modeled infragravity wave spectra at the Aogashima array for January and February 2015. We show (a) 10-hr running mean of measured spectra, (b) output of the combined reflection-gustiness model, (c) output of reflection model, and (d) output of the gustiness model. Averaged spectral quantities are shown in (e) for winter (excluding the event on 21 February) and in (f) for summer.

5. Discussion and Conclusions

The analysis of IG wave measurements (Figure 1) gave strong indications of deep sea IG wave generation. Measurements near the Mediterranean coast of Israel identify an event where IG waves arrived from deep water. Some of the observed IG wave energy may be reflected from far coasts; however, it appears to be too small to account for the entire observed variance of IG waves. The timing and directionality of the most coherent wave rays originating from the Cascadia Array (Neale et al., 2015) coincide with a storm thousand of kilometers offshore. A similar analysis showed the same results using measurements taken in Aogashima station 70 km offshore Japan. These measurements gave evidence of significant deep water offshore IG wave generation.

A new deep sea IG wave mechanism closing a nonlinear resonance condition of wave triads with a wind gustiness component was identified. This mechanism was modeled and implemented to augment a nearshore IG generation-reflection wave model. While there are some discrepancies, a good agreement is found between the envelope of measured IG wave heights and the ones obtained by the combined model of reflection from far coasts augmented by the new model for the Aogashima station measurements (see Figure 2). While some events of high IG wave heights can perhaps be explained as underprediction of the reflection model, in the many of the investigated events there were no strong storm systems that hit far coastlines matching this period (Figures 2c and 2d show values of source terms for rays passing through the storm). The results clearly demonstrate that the additional IG wave energy is proportional to quadratic nonlinear mechanism (E^2) and wind gusts.

In the investigated winter events the new gustiness model provided a significant IG wave energy (sometime in the same order of magnitude of the nearshore generation) with good agreements with measurements. In the investigated summer events, the results of the reflection model generally provided quite good agreements by itself. And indeed, the implementation of the new model did not provide a significant contribution in the summer months and hence no overprediction of IG wave energy. The reflection model is proportional to nearshore wind sea energy H_s, which does not change drastically between the seasons. On the other hand, the square of the wind sea energy in the open ocean ($E^2 \sim H_s^4$) is an order of magnitude higher during winter (see Bromirski et al., 2013). Hence, the influence of the new deep source term on the summer spectrum is minimal, while the influence on the winter spectrum is significant.

The assumptions used in the paper provide a first-order approximation of deep sea IG wave generation. It follows a rationale that is used to account for gust effects on the mean wave growth in operational models. This approach allowed it to provide relatively good agreements to the measurements; however, some discrepancies do exist. Most notably on the 20–21 February, a significant peak of IG energy was observed. During this time a strong storm developed in coastal waters of Japan. These IG waves may have been generated by a mechanism discussed in de Jong and Battjes (2004) or an additional unknown mechanism. An overprediction of IG wave heights on the 45th calendar day of the year (Figure 2) is likely due to the fact that the storm and the IG wave ray directions were mostly orthogonal during this period. This leads to the conclusion that the directional distribution of generated IG waves is not uniform which was taken as a first approximation. Further work on the theory of wave growth under oscillating winds is required to account for such directional IG wave generation.

Additional discrepancies are likely to arise from the fact that IG generation is based on mean wind and wave parameters in a similar fashion to that of Ardhuin et al. (2014; i.e., an even distribution in the directional domain using H_s, D_p, and T_p as wave parameters). The inclusion of various other parameters was considered, and the use of different spectral shapes for gustiness van der Hoven (1957) was also investigated, although the current white noise formulation provided a better agreement in the spectral domain. Finally, difference in growth rate due to gusts was parametrized as a function of mean wind speed only. Nevertheless, the presented simple formulation yielded the most consistent results.

As the effect of gustiness even on the mean wave growth is a complex phenomenon and exact spatiotemporal gustiness properties (magnitude, propagation speeds, etc.) are generally unavailable, it is difficult to investigate IG generation properties in detail. A step forward would be to run a coupled atmospheric and wave action model with a gustiness source term. The presented analysis leads to the conclusion that submesoscale wind variations need to be measured and investigated, as well as the possibility of their implementation into operational wave models.

As shown in Figure 3, the new mechanism mostly contributes to generation of IG waves at higher frequencies. This is also consistent with the Aogashima measurements where the largest underpredictions of the reflection model were in the high-frequency range. The combined reflection-gustiness model is much better at reproducing the measured spectral shapes. The reflection-based model has mostly adequate spectral shapes during the summer, however, even then it has some underprediction at high frequencies and overprediction at low ones. This spectral shape discrepancy can perhaps be explained by the fact that the used discretization step (0.5°) is not sufficient to fully account for refraction effects in the nearshore area. Indeed, it was shown in Smit et al. (2018) that a significant portion of IG wave energy is refractively trapped along continental shelves, which affects lower frequencies more strongly. In addition, the reflection model always assumes the same spectral shape of reflected IG waves (peak at 0.015 Hz), which is not necessarily the case.

In conclusion, measurements and simulations show that deep ocean storms may generate IG waves on different scales and directions (with and opposing direction of wind waves) than previously suggested. The new generation mechanism involves closures of nonlinear Bragg resonance with temporal and spatial inhomogeneities of the medium resulting from wind gusts. Other potential sources of inhomogeneity were considered (not presented here). They include open ocean bathymetry features, mean wave growth, and wave breaking. However, preliminary analysis indicated that wind gusts are the dominant mechanism of IG wave generation in the investigated events.

Indeed, IG wave generation and reflection from coastlines is a major source of deep water IG waves. However, the new mechanism may explain wave generation which cannot be modeled by reflection from coastlines and can also generate IG waves in higher-frequency ranges. Furthermore, depending on the geographical location and season, the gust-generated waves may be the main source of IG energy. The presented work fills a gap in IG wave generation theory and hopefully provides a major step toward a new IG wave forecasting model.

The gust-generated IG waves are relevant not only because of their magnitude but also due to their different frequency range and directionality. As harbor agitations, altimetry measurements, ice-wave interactions, and other physical processes strongly depend on these wave properties, gust-generated IG waves may have a significant importance in various fields.

Acknowledgments
The ERA5 and ERA-Interim reanalysis data, which were used in this paper, are available the following websites (https://cds.climate.copernicus.eu/cdsapp#!/dataset/reanalysis-era5-single-levels?tab=overview) and (https://www.ecmwf.int/en/forecasts/datasets/browse-reanalysis-datasets), respectively. The ETOPO1 bathymetry data sets, provided by the National Centers for Environmental Information, are available online (https://maps.ngdc.noaa.gov/viewers/wcs-client/). ADCP and waveform data used in this paper are publicly available from Yaron Toledo's ResearchGate profile (https://www.researchgate.net/publication/331715699&urluscore;Pressure&urluscore;cell&urluscore;data&urluscore;near&urluscore;Haifa). The hindcast IG wave data are available online (ftp://ftp.ifremer.fr/ifremer/ww3/HINDCAST/GLOBAL&urluscore;IG/). The pressure cell data of the Aogashima array are available online (http://p21.jamstec.go.jp/top/). We thank Dr. Sara Nauri for helpful discussions and comments. We would also like to thank everyone involved in the deployment of the MEP Lab's ADCPs. This research was supported by the ISRAEL SCIENCE FOUNDATION (Grant 1940/14) and Israel's Ministry of Science and Technology (Grant 3-12473). We declare no conflicts of interest.

References

Aagaard, T., & Greenwood, B. (1994). Suspended sediment transport and the role of infragravity waves in a barred surf zone. *Marine Geology*, *118*(1-2), 23–48. https://doi.org/10.1016/0025-3227(94)90111-2

Abdalla, S., & Cavaleri, L. (2002). Effect of wind variability and variable air density on wave modeling. *Journal of Geophysical Research*, *107*(C7), 3080. https://doi.org/10.1029/2000JC000639

Amante, C., & Eakins, B. W. (2009). ETOPO1 arc-minute global relief model: Procedures, data sources and analysis.

Ardhuin, F., Rawat, A., & Aucan, J. (2014). A numerical model for free infragravity waves: Definition and validation at regional and global scales. *Ocean Modelling*, *77*, 20–32. https://doi.org/10.1016/J.OCEMOD.2014.02.006

Aucan, J., & Ardhuin, F. (2013). Infragravity waves in the deep ocean: An upward revision. *Geophysical Research Letters*, *40*, 3435–3439. https://doi.org/10.1002/grl.50321

Bromirski, P. D., Cayan, D. R., Helly, Y., & Wittmann, P. (2013). Wave power variability and trends across the North Pacific. *Journal of Geophysical Research: Oceans*, *118*, 6329–6348. https://doi.org/10.1002/2013JC009189

Bromirski, P. D., Sergienko, O. V., & MacAyeal, D. R. (2010). Transoceanic infragravity waves impacting Antarctic ice shelves. *Geophysical Research Letters*, *37*, L02502. https://doi.org/10.1029/2009GL041488

de Jong, M. P. C., & Battjes, J. A. (2004). Low-frequency sea waves generated by atmospheric convection cells. *Journal of Geophysical Research*, *109*, C01011. https://doi.org/10.1029/2003JC001931

Dee, D. P., Uppala, S., Simmons, A., Berrisford, P., Poli, P., Kobayashi, S., et al. (2011). The era-interim reanalysis: Configuration and performance of the data assimilation system. *Quarterly Journal of the royal meteorological society*, *137*(656), 553–597.

Godin, O. A., Zabotin, N. A., Sheehan, A. F., Yang, Z., & Collins, J. A. (2013). Power spectra of infragravity waves in a deep ocean. *Geophysical Research Letters*, *40*, 2159–2165. https://doi.org/10.1002/grl.50418

Hasselmann, K. (1962). On the non-linear energy transfer in a gravity-wave spectrum. Part 1. General theory. *Journal of Fluid Mechanics*, *12*(04), 481. https://doi.org/10.1017/S0022112062000373

Hasselmann, K., Barnett, T., Bouws, E., Carlson, H., Cartwright, D., Enke, K., et al. (1973). Measurements of wind-wave growth and swell decay during the Joint North Sea Wave Project (JONSWAP). Ergänzungsheft 8-12.

Herbers, T. H. C., Elgar, S., Guza, R. T., Herbers, T. H. C., Elgar, S., & Guza, R. T. (1994). Infragravity-frequency (0.0050.05 Hz) motions on the shelf. Part I: Forced waves. *Journal of Physical Oceanography*, *24*(5), 917–927. https://doi.org/10.1175/1520-0485(1994)024h0917:IFHMOTi2.0.CO;2

Herbers, T. H. C., Elgar, S., Guza, R. T., O'Reilly, W. C., Herbers, T. H. C., Elgar, S., et al. (1995). Infragravity-frequency (0.0050.05 Hz) motions on the shelf. Part II: Free waves. *Journal of Physical Oceanography*, *25*(6), 1063–1079. https://doi.org/10.1175/1520-0485(1995)025h1063:IFHMOTi2.0.CO;2

Janssen, P. (2004). *The interaction of ocean waves and wind*. Cambridge: Cambridge University Press. https://doi.org/10.1017/CBO9780511525018

Longuet-Higgins, M. S., & Stewart, R. W. (1962). Radiation stress and mass transport in gravity waves, with application to surf beats'. *Journal of Fluid Mechanics*, *13*(4), 481. https://doi.org/10.1017/S0022112062000877

Neale, J., Harmon, N., & Srokosz, M. (2015). Source regions and reflection of infragravity waves offshore of the U.S.s Pacific Northwest. *Journal of Geophysical Research: Oceans*, *120*, 6474–6491. https://doi.org/10.1002/2015JC010891

Part VII : ECMWF Wave Model (2018). In Ifs documentation cy45r1. ECMWF.

Rhie, J., & Romanowicz, B. (2006). A study of the relation between ocean storms and the Earth's hum. *Geochemistry, Geophysics, Geosystems*, *7*, Q10004. https://doi.org/10.1029/2006GC001274

Schäffer, H. A. (1993). Infragravity waves induced by short-wave groups. *Journal of Fluid Mechanics*, *247*(-1), 551. https://doi.org/10.1017/S0022112093000564

Simley, E., Pao, L., Kelley, N., Jonkman, B., & Frehlich, R. (2012). LIDAR wind speed measurements of evolving wind fields, *50th AIAA aerospace sciences meeting including the new horizons forum and aerospace exposition* (pp. 1–656). Reston, Virigina: American Institute of Aeronautics and Astronautics. https://doi.org/10.2514/6.2012-656

Smit, P. B., Janssen, T. T., Herbers, T. H. C., Taira, T., & Romanowicz, B. A. (2018). Infragravity wave radiation across the shelf break. *Journal of Geophysical Research: Oceans*, *123*, 4483–4490. https://doi.org/10.1029/2018JC013986

Sugioka, H., Fukao, Y., & Kanazawa, T. (2010). Evidence for infragravity wave-tide resonance in deep oceans. *Nature Communications*, *1*(7), 1–7. https://doi.org/10.1038/ncomms1083

Symonds, G., Huntley, D. A., & Bowen, A. J. (1982). Two-dimensional surf beat: Long wave generation by a time-varying breakpoint. *Journal of Geophysical Research*, *87*(C1), 492. https://doi.org/10.1029/JC087iC01p00492

The Wamdi Group (1988). The WAM model. A third generation ocean wave prediction model. *Journal of Physical Oceanography*, *18*(12), 1775–1810. https://doi.org/10.1175/1520-0485(1988)018h1775:TWMTGOi2.0.CO;2

Thomson, J., Elgar, S., Herbers, T. H. C., Raubenheimer, B., & Guza, R. T. (2007). Refraction and reflection of infragravity waves near submarine canyons. *Journal of Geophysical Research*, *112*, C10009. https://doi.org/10.1029/2007JC004227

Tonegawa, T., Fukao, Y., Shiobara, H., Sugioka, H., Ito, A., & Yamashita, M. (2018). Excitation location and seasonal variation of transoceanic infragravity waves observed at an absolute pressure gauge array. *Journal of Geophysical Research: Oceans*, *123*, 40–52. https://doi.org/10.1002/2017JC013488

Tucker, M. J. (1950). Surf beats: Sea waves of 1 to 5 min. period. *Proceedings of the Royal Society A: Mathematical, Physical and Engineering Sciences*, *202*(1071), 565–573. https://doi.org/10.1098/rspa.1950.0120

Uchiyama, Y., & McWilliams, J. C. (2008). Infragravity waves in the deep ocean: Generation, propagation, and seismic hum excitation. *Journal of Geophysical Research*, *113*, C07029. https://doi.org/10.1029/2007JC004562

van der Hoven, I. (1957). Power spectrum of horizontal wind speed in the frequency range from 0.0007 to 900 cycles per hour. *Journal of Meteorology*, *14*(2), 160–164. https://doi.org/10.1175/1520-0469(1957)014h0160:PSOHWSi2.0.CO;2

Vrecica, T., & Toledo, Y. (2016). Consistent nonlinear stochastic evolution equations for deep to shallow water wave shoaling. *Journal of Fluid Mechanics*, *794*, 310–342. https://doi.org/10.1017/jfm.2015.750

Zhang, Y., Paparis, B., Schäffer, H., & Ostrovsky, D. (2016). Field observations and numerical modeling of infragravity waves at the port of Haifa, Israel. *Ports 2016*, 28–37.